Since January 2020 Elsevier has created a COVID-19 resource centre with free information in English and Mandarin on the novel coronavirus COVID-19. The COVID-19 resource centre is hosted on Elsevier Connect, the company's public news and information website.

Biomedical Signal Processing and Control 79 (2023) 104159

Contents lists available at ScienceDirect

Biomedical Signal Processing and Control

journal homepage: www.elsevier.com/locate/bspc

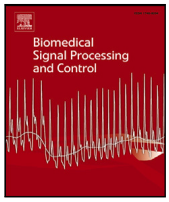

COVID-19 ground-glass opacity segmentation based on fuzzy c-means clustering and improved random walk algorithm

Guowei Wang [a,1], Shuli Guo [a,1], Lina Han [b,*], Zhilei Zhao [a], Xiaowei Song [a]

[a] State Key Laboratory of Intelligent Control and Decision of Complex Systems, School of Automation, Beijing Institute of Technology, Beijing, 100081, China
[b] Department of Cardiology, The Second Medical Center, National Clinical Research Center for Geriatric Diseases, Chinese PLA General Hospital, Beijing, China

ARTICLE INFO

Keywords:
COVID-19
Ground-glass opacity
Fuzzy c-means clustering
Random walk
Snowfall model
Markov random field

ABSTRACT

Accurate segmentation of ground-glass opacity (GGO) is an important premise for doctors to judge COVID-19. Aiming at the problem of mis-segmentation for GGO segmentation methods, especially the problem of adhesive GGO connected with chest wall or blood vessel, this paper proposes an accurate segmentation of GGO based on fuzzy c-means (FCM) clustering and improved random walk algorithm. The innovation of this paper is to construct a Markov random field (MRF) with adaptive spatial information by using the spatial gravity Model and the spatial structural characteristics, which is introduced into the FCM model to automatically balance the insensitivity to noise and preserve the effectiveness of image edge details to improve the clustering accuracy of image. Then, the coordinate values of nodes and seed points in the image are combined with the spatial distance, and the geodesic distance is added to redefine the weight. According to the edge density of the image, the weight of the grayscale and the spatial feature in the weight function is adaptively calculated. In order to reduce the influence of edge noise on GGO segmentation, an adaptive snowfall model is proposed to preprocess the image, which can suppress the noise without losing the edge information. In this paper, CT images of different types of COVID-19 are selected for segmentation experiments, and the experimental results are compared with the traditional segmentation methods and several SOTA methods. The results suggest that the paper method can be used for the auxiliary diagnosis of COVID-19, so as to improve the work efficiency of doctors.

1. Introduction

The pathological features of COVID-19 are complex and difficult to distinguish, with a high speed of transmission, and the early symptoms are difficult to detect [1]. The GGO is a common lesion of COVID-19 [2]. Doctors can diagnose the patient's condition through information such as the size, shape, and texture of the GGO, so as to take treatment for patients in time [3]. In the actual diagnosis, due to the diversity of GGO and the differences in the condition of patients, the number, type, shape, size, density, location and other characteristics of GGO are quite different [4]. Doctors are affected by unstable factors such as the limitation of professional experience, distraction or fatigue, which may lead to the wrong diagnosis for COVID-19 [5,6]. If GGO can be accurately segmented from CT images in the early COVID-19, and then the correct treatment and prognosis are adopted, the infection rate can be reduced by 80% [7]. It can be seen that early and accurate detection of GGO is important for the diagnosis and treatment of COVID-19.

At present, scholars have proposed various solutions for the segmentation of GGO in CT images of COVID-19. Some researchers have proposed a segmentation method that combines the watershed algorithm and the FCM [8]. The center point of the pre-segmented area obtained by FCM are mapped to the corresponding position in the CT image, and the obtained mapping points are used as the seed points to complete the segmentation of the GGO by using the watershed algorithm. Some researchers use the rolling ball algorithm to segment the GGO [9]. The algorithm first preprocesses the lung CT images, then uses the rolling ball method to repair the lung mask, and finally superimposes the images to complete the segmentation of GGO. Some researchers have proposed an improved localized graph-cuts based multiphase active contour model and an improved fuzzy velocity function based on active contour model to separate GGO and isolated GGO respectively [10]. Some researchers use the GGO detection algorithm based on the deep learning [11]. They use the improved convolution neural network to train the dataset, and extract the features such as the

* Corresponding author.
E-mail address: 2438381279@qq.com (L. Han).
[1] These authors contributed equally to this work.

https://doi.org/10.1016/j.bspc.2022.104159
Received 7 April 2022; Received in revised form 10 August 2022; Accepted 4 September 2022
Available online 12 September 2022

size, shape, texture, and then establish a network model to complete the detection and extraction of GGO.

However, these methods are only for the segmentation of specific types of GGO. Since the lung area contains a large number of blood vessels and cohesive GGO, and the pleura has approximately the same gray level as the nodules and blood vessels, the watershed method will mistake the blood vessels and the thorax as GGO, resulting in over-segmentation and false segmentation. Due to the diversity of the size and the shape of GGO, it is difficult to find the structural elements with the same size in the process of rough segmentation caused by blood vessels or nodules by rolling ball method, which reduces the accuracy of segmentation. The segmentation method based on the active contour model cannot achieve a good segmentation effect for GGO due to its sensitivity to the initial contour, low segmentation accuracy and over-reliance on gradient information. Although the detection and segmentation of GGO based on the deep learning can achieve relatively good result, the premise of this algorithm is that it needs to train a large number of annotated datasets, and it takes a lot of time to collect features and algorithm convergence. The algorithm is complex and its calculation is too large.

Recently, the random walk algorithm has achieved a good result in medical image processing [12]. The random walk algorithm based on the graph theory can better identify the weak boundaries while minimizing the risk of the leaking boundaries with simple calculation and fast segmentation [13]. However, the traditional random walk algorithm needs to set a large number of seed points manually, and its application is limited. In view of the above problems, this paper proposes a segmentation of GGO based on FCM clustering and an improved random walk algorithm. The highlights of this paper are as following: (1) the spatial gravity model and the edge coefficient are introduced into the FCM algorithm, and the adaptive spatial information MRF based FCM remote CT image clustering algorithm is proposed. The fuzzy membership degree of FCM is redefined to suppress the gray value of the blood vessel area adhering to the GGO and the edge area, which enhances the contrast between the GGO and the edge. It lays the foundation for the subsequent accurate segmentation. (2) The geodesic distance is added to redefine the weight function of the random walk algorithm, and the shortest weighted distance between the point pairs is used as one of the metrics for segmenting the target area, so as to avoid mis-segmentation caused by the image intensity information. (3) According to the edge density of the image, the proportion of the gray feature and the spatial information in the weight function is adaptively calculated, which is used to replace the weight between adjacent nodes in the traditional random walk algorithm. The gray value and spatial information are effectively fused to realize the adaptive image segmentation. (4) In order to reduce the adverse effect of noise on the image segmentation results, a simulated snowfall algorithm is introduced to preprocess the image. The digital adaptive Gaussian kernel is used to realize the simple snowfall model, and the size, direction and shape of the kernel function are continuously adjusted according to the characteristic information of the image, so as to achieve the purpose of noise suppression without losing rich edge information.

The organization and the structure of this paper are as following: in Sections 2.1 and 2.2, for the initial GGO CT image, the adaptive snowfall model and the improved FCM clustering is proposed for pre-segmentation to enhance the contrast of GGO with high gray value. It reduces the gray level of interference areas such as blood vessels, and then it obtains the coordinates for the GGO pixels. In Sections 2.3 and 2.4, combined with nonlinear anisotropic diffusion filtering and morphological method, the image is filtered and denoised. Under the premise of ensuring a good outline, the irrelevant areas such as noise points and small blood vessels in the lung are removed. In Section 2.5, the seed points required by the random walk algorithm are selected. The spatial geodesic distance between the pixel points and the seed points in the image is added to the random walk algorithm. The shortest geodesic distance between the pixels and seed points in the GGO area is calculated according to the coordinate information, and this distance is used as the measurement basis of the random walk algorithm segmentation, which is used to classify the pixels and realize the accurate segmentation of GGO.

2. GGO segmentation algorithm

2.1. Snowfall model

In the analysis of snowfall model [14], the characteristics of surface are quantified by gradient. In the process of extracting the image segmentation line, the snowfall process is simulated, and the segmentation line is extracted according to the continuous change of the surface curve to realize the image segmentation. The snowfall model simulates the image as the undulating ground, and it simulates the changes of the landmark surface similar to the snowfall process. Because the snowfall model is an adaptive model formed based on the surface conditions, it can be well applied to image segmentation, and it effectively reduces the edge noise and ensure the smoothness of edge segmentation. The snowfall model only optimizes the edge of image segmentation, but it also needs to combine the random walk algorithm to complete the image segmentation. According to the shape and location of GGO, COVID-19 often presents isolated GGO, cohesive GGO attached to the chest wall and pure GGO [15]. Different types of GGO are shown in Fig. 1. The flow chart of the GGO segmentation algorithm proposed in this paper is shown in Fig. 2.

2.1.1. The effect of snow surface

The effect of the snow surface directly affects the vision, and the snow on the object will change the image information of the object in varying degrees. Firstly, the snow will cover some details on the surface of the object. If the image of the object is extracted from the whole, the difficulty of extracting the edge of the object will be reduced, and the entire outline of the object will be highlighted. Secondly, the snow effect can effectively weaken the contrast between the objects. It eliminates unnecessary shadow occlusion and effectively removes noise. Finally, the snowfall not only blurs the details, but also highlights the outline of the large targets.

The surface effect of the snowfall model has a certain relationship with the length of the snowfall time. In the process of setting the snowfall coefficient, it is necessary to not only ensure the snowfall time and suppress the noise as much as possible, but also prevent the snowfall time from being too long to cover useful information. The coefficient of the snowfall is limited by the number of snowfalls.

2.1.2. The contour extraction of lesion based on the snowfall model

The snowfall effect can change the surface profile and simulate the adaptive surface. In this paper, the Gaussian kernel function is used to quantify the surface change of snowfall.

Then, the basic algorithm of Gaussian kernel function will be improved accordingly to better meet the actual image segmentation processing. In order to describe the problem more intuitively, a diagram is used to describe the core idea of the algorithm, as shown in Fig. 3. The standard image is stretched, rotated, and scaled to achieve any image under this transformation. The feature of any image can be jointly represented by the image parameters, including stretching parameters Λ_i, rotation parameters $U_{\theta i}$ and scaling parameters γ_i. Because of this, the feature of any image can be accomplished with an adaptive Gaussian kernel. As shown in Fig. 4, different kernel function shapes are described. Where, (a) is the traditional Gaussian kernel, which describes the flat area in the image, and (b) represents the texture area; (c) represents the weak edge region, (d) represents the strong edge region, and (e) represents the sloped edge region. In order to more intuitively represent the characteristics of these five areas, the classical image analysis is used, as shown in Fig. 5.

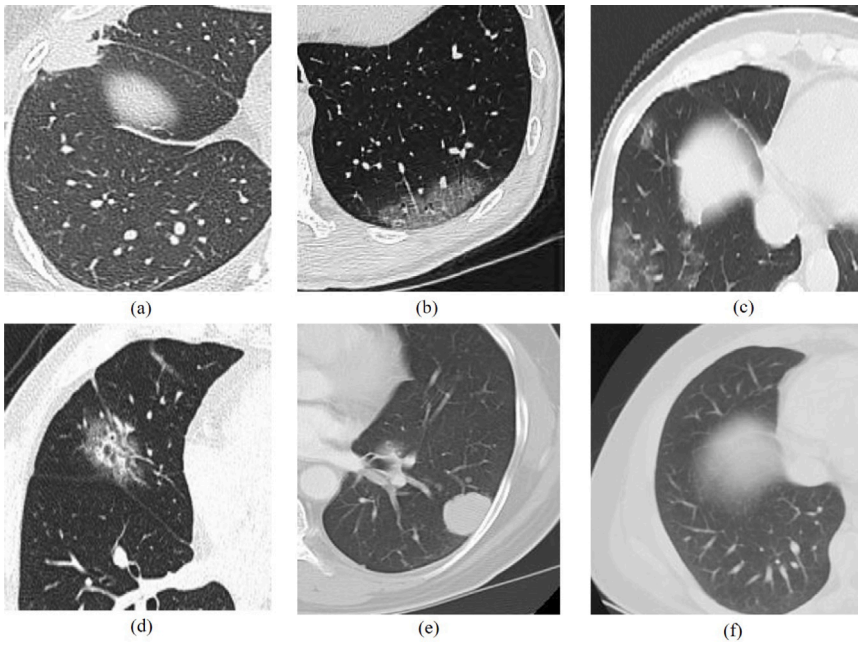

Fig. 1. GGO classification of COVID-19 ((a) vascular adhesive GGO; (b) pleural adhesive GGO; (c) lung wall adhesive GGO; (d) solitary GGO; (e) solid GGO; (f) pure GGO).

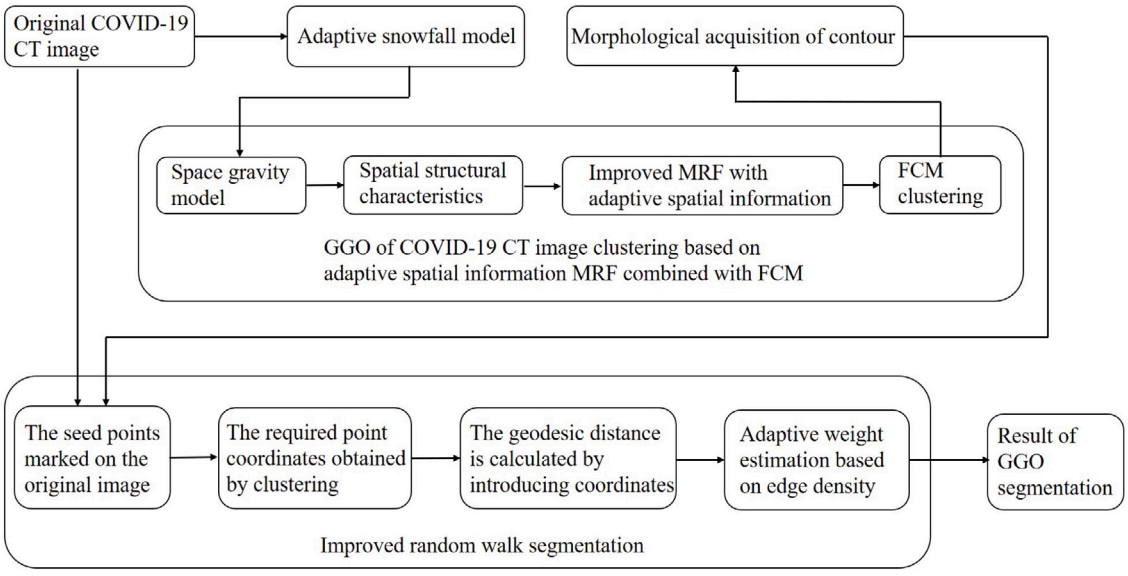

Fig. 2. Flow chart of COVID-19 GGO segmentation.

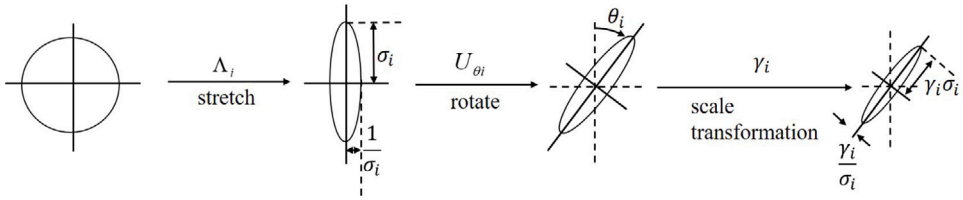

Fig. 3. Improvement of traditional kernel function.

According to the transformation process described above, an adaptive Gaussian kernel function is proposed:

$$k(y, y_0) = exp(-\frac{(y - y_0)^T C_0 (y - y_0)}{2\sigma^2}) \quad (1)$$

where, σ represents the global smoothing factor, $\sigma = 3$. C_0 is the covariance matrix based on local different gray values. In order to simplify the calculation, the eigenvalue decomposed of C_0 is:

$$C_0 = \gamma U_{\theta_0} B_0 U_{\theta_0}^T \quad (2)$$

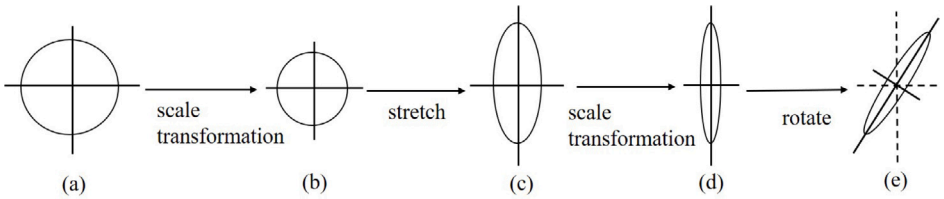

Fig. 4. Adaptive surface evolution kernel ((a) flat region; (b) texture region; (c) weak marginal region; (d) strong marginal region; (e) oblique marginal region).

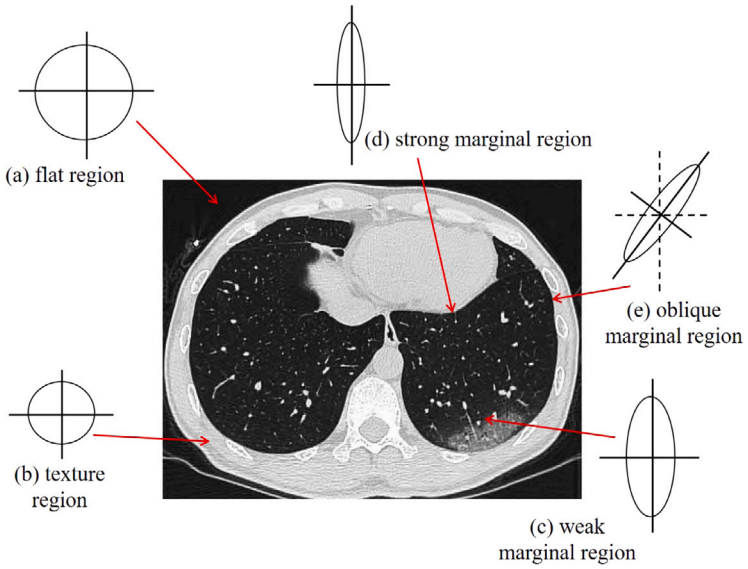

Fig. 5. Diagram of adaptive surface for COVID-19 CT image.

$$U_{\theta_0} = \begin{bmatrix} \cos(\theta_0) & \sin(\theta_0) \\ -\sin(\theta_0) & \cos(\theta_0) \end{bmatrix} \tag{3}$$

$$B_0 = \begin{bmatrix} \sigma_0 & 0 \\ 0 & \sigma_0^{-1} \end{bmatrix} \tag{4}$$

where, C_0, U_{θ_0}, and B_0 represent the rotation matrix, the stretched rectangular matrix and the value of the kernel respectively. The gradient matrix is defined as following:

$$M_0 = U_0 N_0 V_0^T, y_j \in w_0 \tag{5}$$

where, $U_0 N_0 V_0^T$ is the decomposition of M_0, N_0 is the second-order diagonal matrix, which is the value of key direction; $V_0 = [v_1, v_2]^T$ is an orthogonal matrix that defines the direction, the value of angle is:

$$\theta_0 = \arctan(\frac{v_1}{v_2}) \tag{6}$$

The rotation parameter σ_0 is defined according to the gradient direction:

$$\sigma_0 = \frac{v_1 + \eta'}{v_2 + \eta'}, \eta' \geq 0 \tag{7}$$

where, η' is the adjustment factor of stretching, $\eta' = 1$.

The selection factor ϕ_0 is:

$$\phi_0 = (\frac{v_1 v_2 + \eta''}{M})^{1/2} \tag{8}$$

where, η'' is the selection adjustment factor, $\eta'' = 0.01$, $M = 5 \times 5$. The process of adaptive snowfall model is shown in Fig. 6.

In the simulated snowfall model, the adaptive Gaussian kernel function can suppress the noise while enhancing the contour information through a certain number of iterations R with the adaptive rotation parameters σ_0 and the selection factor ϕ_0, which lays a good foundation for the subsequent image segmentation. By controlling the number of iterations R, the snowfall accumulation can be controlled. For the simulated snowfall model, the main factors which affect the number of iterations are the strength of noise, the size of the image and the strength of image edge information. The weak edges require more iterations, and the strong edges require fewer iterations. The larger the noise and the larger the image, the more iterations are required, and vice versa. When the number of iterations is too small, the noise is obvious; when the number of iterations is too many, the edges become blurred. The selection of the number of iterations in this paper mainly depends on the experimental trial and error method. According to the experimental findings, the ideal number R of iterations is 20. The appropriate number of iterations is close to 20, and the change range is not large, which also makes the method of determining the number of iterations through the experiments feasible.

2.2. Adaptive spatial information MRF based FCM remote sensing image clustering algorithm

In this paper, the spatial gravity model and the spatial structure feature are combined to construct the MRF with adaptive spatial information weight, which is introduced into the traditional FCM. This is defined as AMFCM.

2.2.1. MRF with adaptive spatial information

In the traditional MRF in FCM (MFCM) [16], each pixel in the neighborhood has the same influence on the central pixel. It does not take into account the distance between each pixel in the neighborhood and the central pixel. However, according to the first law of geography, the objects with similar spatial distance are more likely to belong to the same type of objects. The closer the neighborhood pixels are to the central pixel, the greater the impact on the central pixel. In addition,

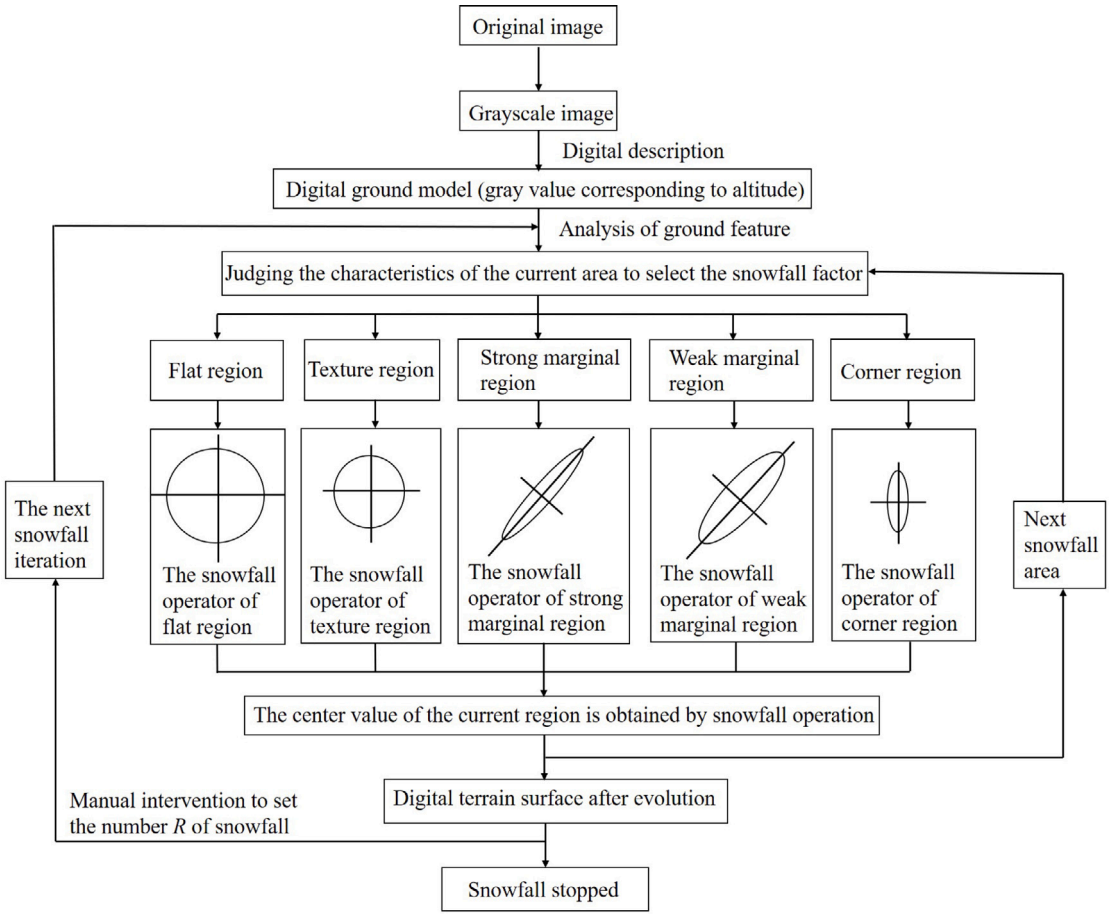

Fig. 6. Flowchart of adaptive snow model.

the clustering effect is not good for complex small target regions in the MFCM model. Therefore, in order to improve the accuracy of clustering, the spatial gravity model and spatial structure feature are introduced to construct the MRF with adaptive spatial information, which describes the weight of spatial information between the central pixel and each pixel in the neighborhood adaptively. It improves the accuracy of clustering for small object regions. According to the space gravity model and the characteristics of space structure, the improved prior probability expression of MRF is:

$$P(ij) = exp(-\alpha(x_i)U(ij))/Z \tag{9}$$

$$Z = \sum_{x \in X} exp(-U(ij)) \tag{10}$$

where, Z is the normalization constant of the segmentation function, $U(ij)$ is the energy function, and its expression is:

$$U(ij) = \sum_{i,j \in C} I(ij) \tag{11}$$

where: $U(ij)$ is the sum of all potential groups in potential group set C. $I(ij)$ is the potential function on C:

$$I(ij) = \begin{cases} -S_{ij} & c(x_i) = c(x_j) \\ 0 & c(x_i) \neq c(x_j) \end{cases} \tag{12}$$

where: $c(x_i)$ is the category of pixel x_i, $c(x_j)$ is the neighborhood category of pixel x_j, and S_{ij} is the spatial attraction between the central pixel x_i and the neighborhood pixel x_j, which is used to control the influence of the neighborhood pixel on the central pixel. α is the feature of spatial structure, which is the edge coefficient of structure.

2.2.2. The model of space gravity

The spatial gravity model is proved to be effective in characterizing the spatial correlation between the image pixels [17]. For two pixels x_i and x_j, their attraction to the kth cluster is directly proportional to their fuzzy membership u_{ik} and u_{jk}. w_{ij} is the weight of the distance between different pixels. Therefore, the pixel spatial attraction S_{ij} between two pixels can be described as:

$$S_{ij} = \frac{w_{ij}}{\sum_{j \in N_i} w_{ij}} \times u_{ik} \times u_{jk} \tag{13}$$

where: $S_{ij} \in (0, 1)$, i is the position of the central pixel. $j \in N_{i,j}\{j = 0, 1, 2, \ldots, 7\}$ is the neighborhood pixel of i. w_{ij} is the weight of the distance between the central pixel and the neighboring pixels, which is the reciprocal of the Euclidean distance, as shown in Fig. 7. Fig. 7 is the square neighborhood system, whose scale is 3. The spatial attraction in Fig. 7(a) exists only between the central pixel and its neighborhood pixel in the given window. And other pixels outside the window are too far away from the central pixel to give any gravity to the central pixel.

2.2.3. Spatial structure characteristics

The edge feature is one of the characteristics of spatial structure [18]. The calculation of gradient is the most common method in edge detection [19]. The Sobel operator is used to calculate the horizontal and vertical gradients of each pixel for the original medical CT image. The gradient expression for each pixel is as following:

$$\nabla x_i = \frac{1}{2}\sqrt{(\nabla^h x_i^j)^2 + (\nabla^v x_i^j)^2} \tag{14}$$

where, $\nabla^h x_i^j$ and $\nabla^v x_i^j$ are the first-order horizontal and vertical gradients of pixel x_i in the jth band respectively. The edge coefficient

$N_{i,0}$	$N_{i,1}$	$N_{i,2}$
$N_{i,3}$	i	$N_{i,4}$
$N_{i,5}$	$N_{i,6}$	$N_{i,7}$

(a)

$1/\sqrt{2}$	1	$1/\sqrt{2}$
1	i	1
$1/\sqrt{2}$	1	$1/\sqrt{2}$

(b)

Fig. 7. The spatial gravity between the central pixel and the neighborhood pixel ((a) neighborhood of central pixel; (b) The distance weight coefficient between the center pixel and the neighborhood pixel).

is constructed, which is expressed as:

$$\alpha(x_i) = \frac{1}{1 + \bigtriangledown x_i} \tag{15}$$

The gradient reciprocal smooth method can not only effectively reduce noise, but also preserve the certain edge and the detail information.

2.2.4. The objective function of AMFCM is constructed

AMFCM is an unsupervised clustering algorithm, which is used for lesion clustering of CT image. It not only combines the local spatial information with grayscale information into the objective function of traditional FCM, but also adds the spatial structure features to reduce noise. At the same time, the accuracy of classification for linear features is improved. Through the MRF of adaptive spatial information, the prior probability P_{ij} of pixel x_i at a certain mark is obtained, and the rejection degree of the mark is obtained. The objective function J_{AMFCM} is obtained by combining the rejection degree with the traditional FCM algorithm. The expression is:

$$J_{AMFCM} = \sum_{i=1}^{N}\sum_{k=1}^{C} u_{ik}^{m}(1 - P(ij))\|x_i - \upsilon_k\| \tag{16}$$

Similarly, according to the Lagrange multiplier method, the necessary conditions for the objective function J_{AMFCM} to obtain the conditional extreme value are:

$$\upsilon_k = \frac{\sum_{i=1}^{N} u_{ik}^{2}(1 - P(ij))x_i}{\sum_{i=1}^{N} u_{ik}^{2}(1 - P(ij))} \tag{17}$$

$$u_{ik} = S_{ij} \times \frac{\|x_i - \upsilon_k\|^{-2}(1 - P(ij))^{-2}}{\sum_{t=1}^{c} \|x_i - \upsilon_t\|^{-2}(1 - P(ij))^{-2}} \tag{18}$$

where, x_i is the gray value of the pixel at the position i; N is the total number of pixels in the CT image; P_{ij} is the prior probability of the MRF; C is the number of clustering; υ_k is the clustering center of the class k; u_{ik} is the membership degree of pixel point i belonging to the class k; m is a constant, which can be used to control the fuzzy degree $m \in (1, \infty)$ of the clustering results. When the parameter m is close to 1, the FCM algorithm tends to be the hard clustering algorithm, which is the same as k-means. When the parameters are close to positive infinity, the entire data tends to be classified into one category. In this paper, $m = 2$, $N = 512 \times 512$.

The improvement of FCM clustering algorithm is shown in Fig. 8. In Fig. 8a, A-D is the vascular region and E-M is the GGO region. When the gray value of the blood vessel area is close to that of the GGO area, it is easy to produce over-segmentation. When the adaptive spatial information weight coefficient is added, the contrast between the blood vessel and the background is reduced, as shown in A-D in Fig. 8b. The closer a pixel is to the vascular region, the smaller the fuzzy membership u_{ik} is. When the pixel belongs to the vascular region, the minimum value is obtained, while the fuzzy membership of the non-vascular region remains almost unchanged. Finally, the GGO is accurately segmented, as shown in E-M in Fig. 8b. In this paper, when using FCM clustering to pre-segment the image, $C = 5$ is set can obtain better processing results, which is conducive to further image processing.

2.2.5. Time computational complexity of the improved FCM clustering algorithm

For the time computational complexity, $O(f)$ is set as the time computational complexity in each iteration of each clustering center, then it can be seen that the time computational complexity of the traditional FCM algorithm [20] is $O(T \cdot H \cdot f)$. Where, T is the total number of iteration and H is the total number of the clustering center. For the traditional FCM, the value of the membership function in each iteration remains unchanged, so there is $O(f_1) = O(f_2) = \cdots = O(f_T) = O(f)$. For the proposed FCM algorithm, since $S_{ij} \in (0, 1)$, the value of the membership function gradually decreases with the increase of iteration, so there is $O(f_1) \geq O(f_2) \geq \cdots \geq O(f_T)$. It can be seen from the above analysis that compared with the traditional FCM, the proposed FCM greatly reduces the time computational complexity.

2.3. Anisotropic diffusion filtering

In the lung CT image, due to the high gray difference between the chest wall area and both sides, in the process of filtering and denoising the lung CT image using the P-M model, the smooth denoising can be carried out in the lung area, while smoothing can be suppressed where there are edges [21,22]. Compared with Gaussian filtering, mean filtering and other methods, on the premise of ensuring the important feature information of the image, it can remove the noise and preserve the image edge more effectively [23,24]. The nonlinear anisotropic diffusion equation is:

$$\begin{cases} \frac{\partial u(x,y,t)}{\partial t} = div(c(x,y,t)\bigtriangledown u) \\ u|_{t=0} = u_0 \end{cases} \tag{19}$$

where, $u(x, y, t)$ represents the image to be processed; div represents the divergence; $\bigtriangledown$ represents the gradient operator; $c(x, y, t)$ represents the diffusion coefficient, which controls the diffusion rate. The image gradient function is usually selected, so that the image edge information can be protected during diffusion. $u(x, y, t) = u_0$ represents the initial condition.

The P-M edge stop function is defined as:

$$c(\|\bigtriangledown u\|) = \frac{1}{1 + (\frac{\|\bigtriangledown u\|}{K})^2} \tag{20}$$

where, the constant K is used to control the sensitivity of the edge, and the image is smooth denoised by iteration. According to several groups of experimental tests, the higher the number of iterations, the better the effect, but the time will increase accordingly. In this paper, the constant K is 0.2 and the number of iterations is 100.

2.4. Morphological method

In this paper, morphological open operation [25,26] and closed operation [27] are combined to remove the interference of noise and other isolated small areas according to the characteristics of target and noise.

2.5. Improved random walk algorithm

In this paper, the random walk algorithm [28] is improved, and the geodesic distance is used as the measurement basis for GGO segmentation, so as to more accurately determine the probability that a pixel belongs to a certain type of seed point. There are many blood vessel areas and edge burr with similar gray values to GGO in CT images of COVID-19, even the GGO adheres to the chest wall. These situations make the random walk algorithm based on gray or Euclidean distance unable to achieve good segmentation results. However, the geodesic distance on the segmentation graph is not limited by this.

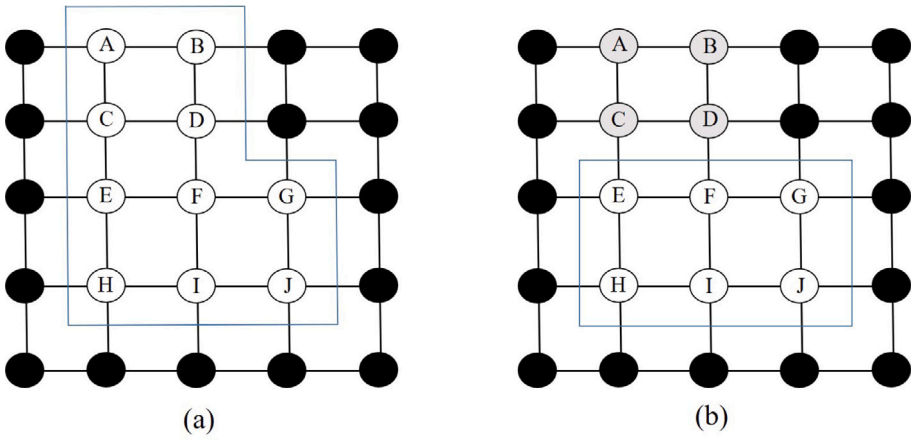

Fig. 8. Improved FCM clustering algorithm ((a) traditional FCM clustering; (b) adding adaptive spatial information characteristic coefficient).

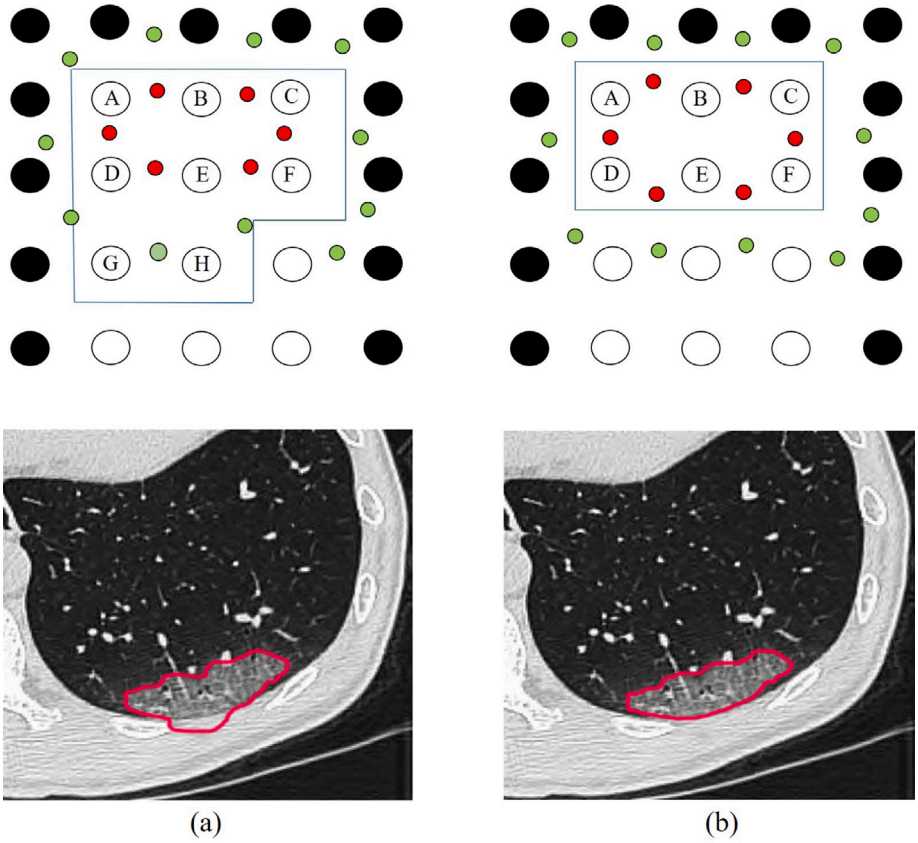

Fig. 9. Comparison of Random Walk Algorithm ((a) Traditional random walk algorithm; (b) Improved random walk algorithm).

2.5.1. Definition of spatial geodetic

In the CT images of COVID-19, the gray value of GGO is almost the same as that of the chest wall. It is difficult to accurately separate the GGO from the chest wall if only based on the gray value information. Therefore, based on the pixel grayscale information, this paper adds the coordinate position information of each pixel and the geodesic distance information between the seed points into the weight function. The geodesic distance between the pixel points and the seed points in the image is defined. It uses coordinate information to calculate geodesic distance. Then the GGO is segmented more accurately according to the image gray level and the spatially shortest geodesic distance.

We define the geodesic distance between the pixel point v_i and the seed point v_k as:

$$D(v_i, v_k) = \min_{P \subset P_{ik}} \sum_{l=1}^{n} \sum_{m=1}^{n} u_{lm} d(x_l, x_m) \tag{21}$$

where, $u_{lm} = \begin{cases} 1, & d_{lm} \in p \\ 0, & d_{lm} \notin p \end{cases}$, it indicates that the path p is connected through the pixel v_i and the seed point $v_k u_{lm} = 1$, otherwise $u_{lm} = 0$, and $p \in P_{ik}$. P_{ik} represents the set of whole paths connecting the pixel points v_i and the seed points v_k. p is the path formed by overlaying a series of edges between the adjacent pixels. That is, the geodesic distance is the shortest path connecting two points in space. The geodesic distance

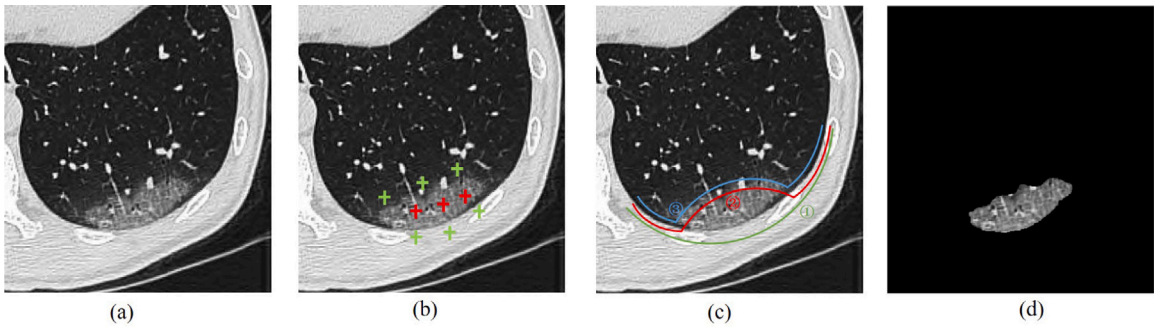

Fig. 10. Seed points selection of random walk ((a) Original CT image; (b) Seed points marked; (c) Selection of seed points; d. Result of GGO segmentation).

preserves the internal geometry of data better than Euclidean distance on a global basis.

The similarity of spatial geodetic between the pixel points v_i and the seed points v_k in the image is defined as:

$$G_{v_i v_k} = exp(-\partial \times \frac{D(v_i, v_k)}{\max_{i=1}^{N} P_{ik}}) \tag{22}$$

2.5.2. The estimation of adaptive weight

The random walk algorithm is an image segmentation method based on the graph structure. The weight function describes the similarity between different nodes and it determines the quality of the image segmentation. This paper proposes an adaptive weight function, which calculates the proportion of grayscale and texture features in the weight function according to the edge density of the image. The similarity description between nodes can better reflect the essential properties of the image. The improved weight function is defined as following:

$$w_{ij} = exp(-\alpha\sqrt{|g_i - g_j|} - (1-\alpha)(\sqrt{|h_i - h_j|} + \max_{k=1}^{N} G_{v_i v_k})) \tag{23}$$

where, g_i represents the gray value of the image pixel i after the snowfall model processing, h_i represents the corresponding gradient value, α represents the parameter of gray feature, $(1-\alpha)$ represents the weight of spatial geodesic distance.

The edge is an important information in the image and it reflects the essential properties of the image. In this paper, the edge density is used to calculate the weight factor α. The calculation of the edge density needs to use the gradient amplitude information of the image. The Sobel operator is used to calculate the gradient amplitude of the image. Corresponding to the input image I, the gradient image is calculated by Eq. (24):

$$E_{i,j} = \sqrt{(E_{i,j}^x)^2 + (E_{i,j}^y)^2} \tag{24}$$

where, $E_{i,j}^x$ and $E_{i,j}^y$ are the gradient values in horizontal and vertical directions respectively, which can be calculated in Eqs. (25) and (26):

$$E_{i,j}^x = (I * S^x)_{i,j} \tag{25}$$

$$E_{i,j}^y = (I * S^y)_{i,j} \tag{26}$$

where, S^x and S^y are the horizontal and vertical Sobel filters respectively. The calculation of the edge density with the node as the center and the fixed size of window is as following:

$$\rho_{i,j} = \frac{\sum_{l=j-n/2}^{j+n/2} \sum_{k=i-m/2}^{i+m/2} E_{k,l}}{m \times n} \tag{27}$$

where: m and n are the length and width of the window respectively, $m = 5$, $n = 5$; the numerator represents the edge strength of nodes in the fixed-size window, and the denominator represents the number of pixels contained in the window. The weight factor α is defined as following:

$$\alpha = \begin{cases} 0, & \rho_{i,j} \ and \ \rho_{k,l} \geq T_1 \\ 1, & \rho_{i,j} \ or \ \rho_{k,l} \leq T_2 \\ \frac{T_1 - max(\rho_{i,j}, \rho_{k,l})}{T_1 - T_2}, & others \end{cases} \tag{28}$$

where, $0 \leq T_1, T_2 \leq 1$. In this paper, when $T_1 = 0.7$ and $T_2 = 0.3$, the adaptive weight function can more accurately reflect the difference between nodes. The size of the weight factor α reflects the complexity of the image neighborhood structure and it determines the proportion of the two weight components in the adaptive weight function. When the neighborhood of image is relatively smooth, the α is relatively large, and the gray-scale similarity weight component in the weight function accounts for the main part. When the image neighborhood structure is relatively complex, the α is relatively small, and the texture similarity weight component in the weight function dominates part, the obtained weight function accurately reflects the structural information of the image, which is beneficial to improve the accuracy of image segmentation.

Fig. 9 shows the different segmentation results before and after the improvement of the random walk algorithm, where the red points are the target seed points and the green points are the background seed points. Before adding the geodesic distance, the GGO is segmented according to the gray information of the image. Due to the similar gray value between the chest wall and GGO, a better segmentation result cannot be obtained, as shown in the left side of Fig. 9. After adding the geodesic distance, the geodesic distance between the image pixel points and the seed points is judged at the adhesion of the chest wall. The connection paths between the pixels in the GGO area and the target seed points are all inside the GGO, while the distance between the background seed points and the pixels outside the target seed point is much larger, so there will be none over-segmentation, as shown on the right side of Fig. 9.

2.5.3. Seed points selection of random walk

Since random walk is an interactive image segmentation algorithm, it is necessary to specify a certain number of seed points in advance. The number of seed points will directly affect the segmentation effect. Too few seed points lead to inaccurate image segmentation. Too many seed points make the segmentation result depends too much on the initial contour target obtained by the mixed Gaussian background modeling (because these seed points will define the label according to the initial contour target), which affects the optimization effect. Therefore, an appropriate number of seed points is beneficial for image segmentation. Aiming at the segmentation problem of different types of GGO, this paper adds the spatial information between image point pairs to the weight function of random walk. Combined with the grayscale information of the pixels, the spatial distance between the pixel points and the seed points in the image is used to complete the segmentation. In adhesive GGO with great difficulty in segmentation, the target seed points in the GGO adhered to the chest wall is marked, as shown by the

red points in Fig. 10b. Then, the background seed points are set at the position of the adhesion chest wall and the low gray level area of lung parenchyma, as shown by the green points in Fig. 10b. It makes full use of the spatial relationship between the image pixels and the seed points. Therefore, when selecting the seed points, the preprocessed image is morphologically expanded with appropriate size, and the contour of lung parenchyma edge is larger than its real contour, as shown by the green line in Fig. 10c. Selecting the edge pixels as the background seed points, and the required coordinate values are recorded. Morphological erosion of appropriate size is then performed, and the margin of the lung parenchyma is still larger than its true contour at this time, as shown by the red line in Fig. 10c. Selecting the edge pixels as the target seed points can ensure that there exists the target seed points in the GGO area, and the required coordinate values are recorded. Finally, the large-scale morphological erosion is carried out, then the edge contour of lung parenchyma is smaller than its real contour, as shown in blue line in Fig. 10c. The edge pixels are selected as the background seed points, and the seed points must be outside the GGO and inside the lung parenchyma. After the seed points are obtained, the improved random walk algorithm is used to calculate the geodesic distance between the pixel points required for segmentation and the seed points, so as to complete the accurate segmentation of the GGO. The segmentation result is shown in Fig. 10d.

3. Analysis of experimental results and performance

Aiming at the different kinds of GGO COVID-19 CT images including vascular adhesive GGO, pleural adhesive GGO, lung wall adhesive GGO, solitary GGO, solid GGO, pure GGO are tested by the Intel E8200 CPU 2.5 GHz, RAM 8G, Matlab 2016a. The size of the image is 512 × 512. The COVID-19 CT images tested in this paper are from COVID-19 CT segmentation dataset (https://medicalsegmentation.com/covid19/) and LIDC-IDRI (https://paperswithcode.com/dataset/lidc-idri). This paper calculates the Dice similarity coefficient (DSC) and sensitivity of image segmentation effect to verify the effectiveness of the experimental methods. The Dice similarity coefficient can be obtained by measuring the overlap between the segmentation results of the paper method and the manual segmentation results of experts, namely:

$$DSC = \frac{2 \times |u \cap v|}{|u| + |v|} \tag{29}$$

where, u represents the segmentation result of this article, and v represents the golden standard segmentation result by doctor.

The $sensitivity$ is obtained by measuring the ratio of the segmentation results of the paper method and the expert manual segmentation results to correctly segment the GGO area, namely:

$$Sensitivity = \frac{|u \cap v|}{|u|} \tag{30}$$

where, u represents the segmentation result of this article, and v represents the golden standard segmentation result by doctor. This paper compares with the comparative methods and uses the accuracy IOU index to objectively evaluate the experimental results:

$$IOU = \frac{N_{11} + N_{10}}{N_{11} + N_{10} + N_{01} + N_{00}} \tag{31}$$

where, N_{11} represents the correctly segmented GGO region. N_{10} represents the correctly segmented background region. N_{01} represents the incorrectly segmented GGO region and N_{00} represents the incorrectly segmented background region. The greater the accuracy IOU, the more accurate the image segmentation is and the closer to the standard segmentation.

Golden standard segmented GGO by doctor (GSSD), improved random walk combined with traditional FCM (IRWF) [29], watershed image segmentation (WIS) [8], automatic random walk image segmentation (ARW) [30], traditional random walk image segmentation (TRWS) [31], region growth combined with morphological (RGCM) [32], super-pixel random walk image segmentation (SRWS) [33], adaptive spatial information MRF combined with FCM and improved random walk algorithm (AMFRW, paper method) are used for simulation comparison tests.

Table 1
Comparison of AMFRW with different methods for COVID-19 CT image of vascular adhesive GGO.

Segmentation method	Dice	Sensitivity	IOU
AMFRW	**0.964**	**0.953**	**0.957**
IRWF	0.876	0.885	0.864
RGCM	0.852	0.866	0.842
SRWS	0.849	0.851	0.839
ARW	0.813	0.826	0.801
TRWS	0.781	0.797	0.775
WIS	0.757	0.762	0.742

It can be seen from Fig. 11 that the algorithm in this paper has better segmentation result than the comparison methods on different types of GGO in COVID-19. Since the comparison methods only consider the grayscale information between pixels, it cannot achieve better segmentation result for different kinds of GGO with small difference of grayscale. Fig. 11(c1)–(i6) show the segmentation results of AMFRW, IRWF, RGCM, SRWS, ARW, TRWS, and WIS for different types of GGO respectively. Among them, Fig. 11(c1)–(c6) show the best segmentation results of AMFRW (paper method). Visually, the segmentation effect of AMFRW is better due to the application of spatial information. Different types of GGO are segmented as lesions to a certain extent. In the comparison methods, due to the inhomogeneity of GGO, it has similar gray value with the surrounding lung wall, blood vessels, pleura, etc. A good segmentation result cannot be obtained only by the segmentation method of grayscale information. For example, in Fig. 11(h1), it can be found that the GGO segmentation result contains some blood vessels, which is inconsistent with the actual situation. By comparing Fig. 11(c2) and (i2), it can be seen that the GGO segmentation effect of Fig. 11(c2) is better than that of Fig. 11(i2). The edge of GGO in Fig. 11(i2) is not obvious, and the segmentation effect is not good for the state of pleural adhesion. The reason is that the segmentation result of the traditional method is isotropic, which makes the segmentation result lose the details of the GGO. In Fig. 11(c2), this situation is changed because the spatial correlation of pixels is considered. The algorithm in this paper redefines the weight function of the random walk, and it adds the spatial geodetic distance between the pixel points and the seed points to the measurement of the segmentation process, which can complete the accurate segmentation of different types of GGO, making the segmentation results closer to the real target area. The FCM algorithm with adaptive spatial information weight coefficient can enhance the contrast of GGO region compared to the background and suppress the gray value of the edge-independent area. It can better deal with the over-segmentation caused by blood vessels, burrs and other factors.

The improved segmentation method in this paper has better indicators for the DSC and the $sensitivity$. The segmented GGO image can fully and clearly show the lesions, which is helpful to improve the accuracy and sensitivity of COVID-19 classification. The extraction of GGO for different kinds of COVID-19 CT images are shown in Fig. 11. The calculation results are shown in Tables 1–6. Table 7 is the average of GGO segmentation results for comparison of AMFRW with different methods. From the change trend of the data in Table 7, compared with the comparative segmentation methods, AMFRW has increased the value of $Dice$ about 0.086, the value of $Sensitivity$ has been increased by about 0.076, the value of IOU has been increased by about 0.095. It can be seen that the segmentation effect for different kinds of GGO under AMFRW is the best.

We compared the AMFRW with 9 state-of-the-art approaches including Inf-Net [34], Chain code-SVM [35], CNN-Clustering [36],

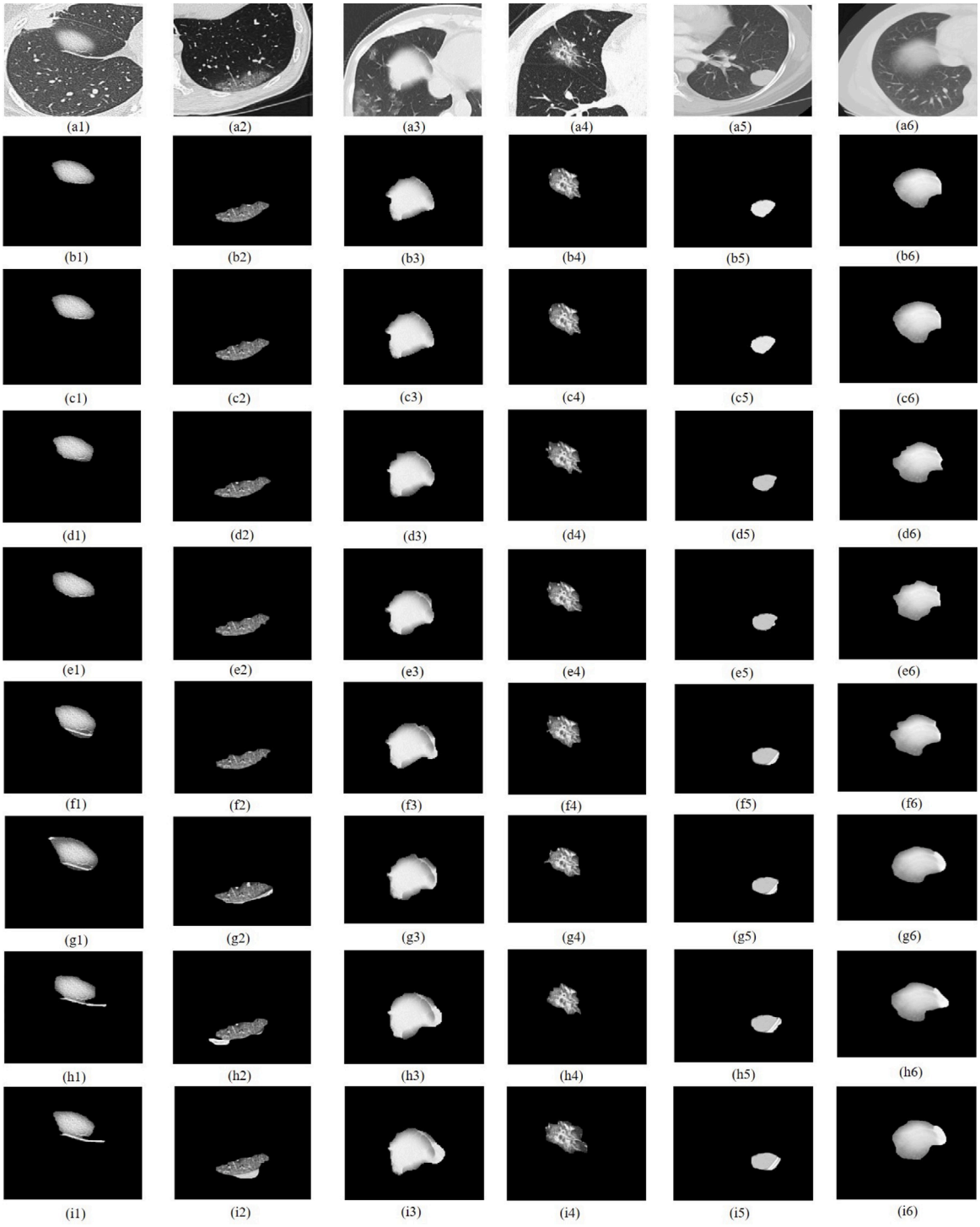

Fig. 11. COVID-19 CT image of vascular adhesive GGO: (a1) original CT image; (b1) segmented by doctor(golden standard); (c1) segmented by AMFRW(paper method); (d1) segmented by IRWF; (e1) segmented by RGCM; (f1) segmented by SRWS; (g1) segmented by ARW; (h1) segmented by TRWS; (i1) segmented by WIS. COVID-19 CT image of pleural adhesive GGO: (a2) original CT image; (b2) segmented by doctor(golden standard); (c2) segmented by AMFRW(paper method); (d2) segmented by IRWF; (e2) segmented by RGCM; (f2) segmented by SRWS; (g2) segmented by ARW; (h2) segmented by TRWS; (i2) segmented by WIS. COVID-19 CT image of lung wall adhesive GGO: (a3) original CT image; (b3) segmented by doctor(golden standard); (c3) segmented by AMFRW(paper method); (d3) segmented by IRWF; (e3) segmented by RGCM; (f3) segmented by SRWS; (g3) segmented by ARW; (h3) segmented by TRWS; (i3) segmented by WIS. COVID-19 CT image of solitary GGO: (a4) original CT image; (b4) segmented by doctor(golden standard); (c4) segmented by AMFRW(paper method); (d4) segmented by IRWF; (e4) segmented by RGCM; (f4) segmented by SRWS; (g4) segmented by ARW; (h4) segmented by TRWS; (i4) segmented by WIS. COVID-19 CT image of solid GGO: (a5) original CT image; (b5) segmented by doctor(golden standard); (c5) segmented by AMFRW(paper method); (d5) segmented by IRWF; (e5) segmented by RGCM; (f5) segmented by SRWS; (g5) segmented by ARW; (h5) segmented by TRWS; (i5) segmented by WIS. COVID-19 CT image of pure GGO: (a6) original CT image; (b6) segmented by doctor(golden standard); (c6) segmented by AMFRW(paper method); (d6) segmented by IRWF; (e6) segmented by RGCM; (f6) segmented by SRWS; (g6) segmented by ARW; (h6) segmented by TRWS; (i6) segmented by WIS.

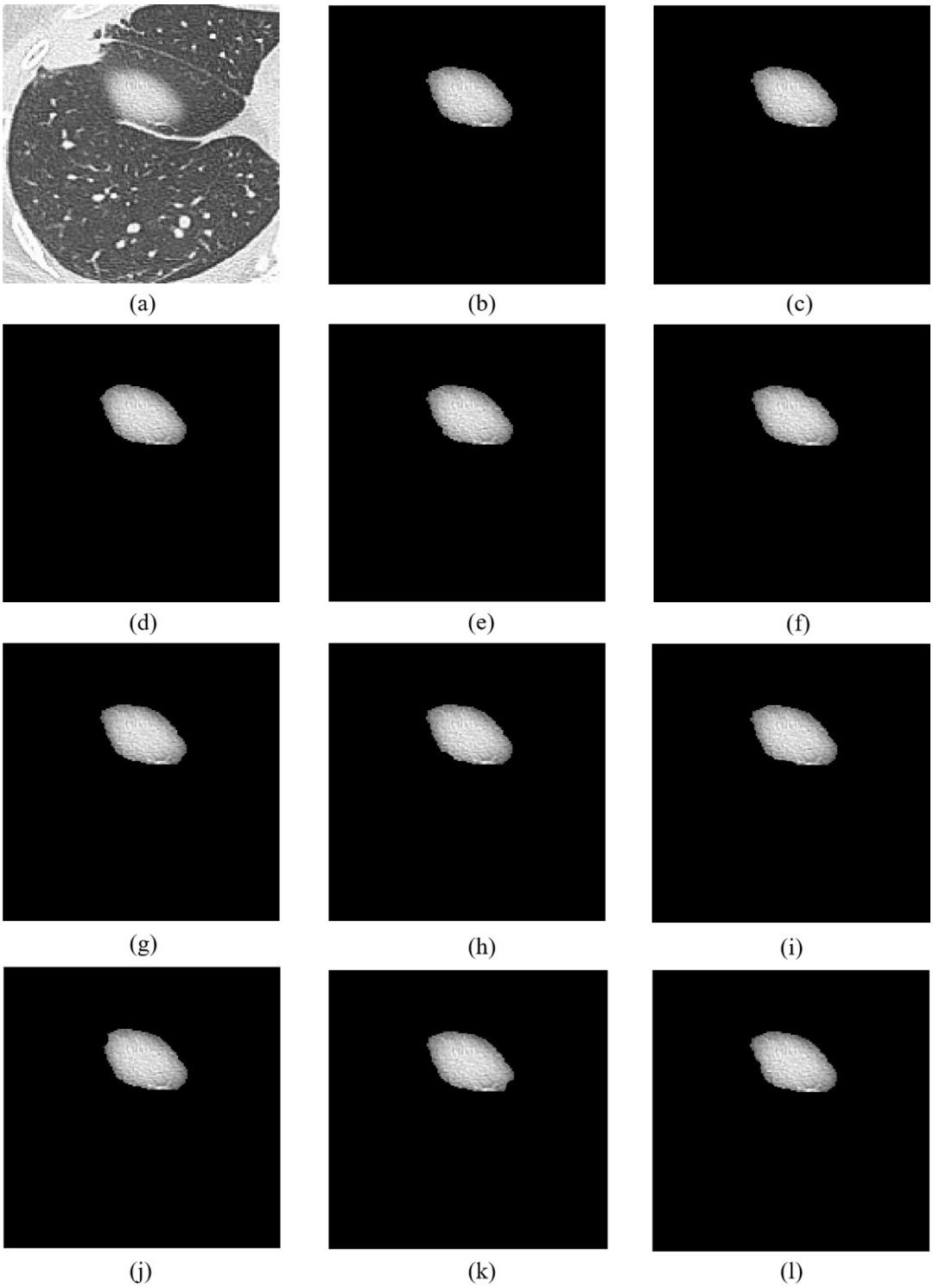

Fig. 12. COVID-19 CT image of vascular adhesive GGO: (a) original CT image; (b) segmented by doctor(golden standard); (c) segmented by AMFRW(paper method); (d) segmented by GAN-Unet; (e) segmented by U-Net++; (f) segmented by MLT; (g) segmented by CNN-Clustering; (h) segmented by Chain code-SVM; (i) segmented by Inf-Net; (j) segmented by R2U-Net; (k) segmented by FCN; (l) segmented by CPMC.

MLT [37], GAN-Unet [38], U-Net++ [39], R2U-Net [40], FCN [41], and CPMC [42] to do segmentation simulations on the COVID-19 CT image of vascular adhesive GGO, and further comparing and analyzing the $Dice$, $Sensitivity$ and IOU under different segmentation methods. The comparative COVID-19 CT image segmentation simulations of vascular adhesive GGO are shown in Fig. 12. The evaluation index values are shown in Table 8.

From the change trend of the data in Table 8, compared with the comparative segmentation methods, AMFRW has increased the value of $Dice$ about 0.008, the value of $Sensitivity$ has been increased by about 0.005, the value of IOU has been increased by about 0.008. It can be seen that the segmentation effect for the COVID-19 CT image of vascular adhesive GGO under AMFRW is the best. It can better deal with the over-segmentation caused by blood vessels, burrs and other

Table 2
Comparison of AMFRW with different methods for COVID-19 CT image of pleural adhesive GGO.

Segmentation method	Dice	Sensitivity	IOU
AMFRW	**0.956**	**0.973**	**0.946**
IRWF	0.883	0.905	0.874
RGCM	0.867	0.882	0.852
SRWS	0.854	0.871	0.841
ARW	0.812	0.836	0.807
TRWS	0.790	0.812	0.783
WIS	0.753	0.761	0.739

Table 3
Comparison of AMFRW with different methods for COVID-19 CT image of lung wall adhesive GGO.

Segmentation method	Dice	Sensitivity	IOU
AMFRW	**0.934**	**0.942**	**0.957**
IRWF	0.883	0.904	0.913
RGCM	0.857	0.875	0.882
SRWS	0.844	0.862	0.871
ARW	0.823	0.841	0.856
TRWS	0.782	0.806	0.813
WIS	0.769	0.782	0.792

Table 4
Comparison of AMFRW with different methods for COVID-19 CT image of solitary GGO.

Segmentation method	Dice	Sensitivity	IOU
AMFRW	**0.964**	**0.956**	**0.963**
IRWF	0.903	0.894	0.905
RGCM	0.876	0.863	0.872
SRWS	0.852	0.846	0.854
ARW	0.838	0.822	0.833
TRWS	0.822	0.814	0.822
WIS	0.792	0.780	0.791

Table 5
Comparison of AMFRW with different methods for COVID-19 CT image of solid GGO.

Segmentation method	Dice	Sensitivity	IOU
AMFRW	**0.976**	**0.968**	**0.962**
IRWF	0.894	0.885	0.884
RGCM	0.873	0.864	0.866
SRWS	0.857	0.843	0.847
ARW	0.844	0.832	0.836
TRWS	0.823	0.816	0.819
WIS	0.802	0.794	0.797

Table 6
Comparison of AMFRW with different methods for COVID-19 CT image of pure GGO.

Segmentation method	Dice	Sensitivity	IOU
AMFRW	**0.955**	**0.967**	**0.959**
IRWF	0.884	0.894	0.885
RGCM	0.867	0.873	0.863
SRWS	0.833	0.848	0.832
ARW	0.802	0.813	0.808
TRWS	0.788	0.792	0.784
WIS	0.762	0.771	0.762

factors, which reduces the mistake diagnosis for the vascular adhesive GGO.

4. Conclusion

This paper proposes an accurate segmentation of GGO based on FCM clustering and improved random walk algorithm. Firstly, the combination of random walk and snowfall model improves the performance of image segmentation, especially in the edge processing, which not only maintains the original characteristics of the image, but also

Table 7
The average of GGO segmentation results for comparison of AMFRW with different methods.

Segmentation method	Dice	Sensitivity	IOU
AMFRW	**0.958**	**0.959**	**0.956**
IRWF	0.872	0.883	0.861
RGCM	0.854	0.863	0.843
SRWS	0.842	0.847	0.834
ARW	0.816	0.833	0.817
TRWS	0.776	0.811	0.788
WIS	0.753	0.771	0.764

Table 8
Comparison of AMFRW with different SOTA methods for COVID-19 CT image of vascular adhesive GGO.

Segmentation method	Dice	Sensitivity	IOU
AMFRW	**0.964**	**0.953**	**0.957**
GAN-Unet	0.956	0.948	0.949
U-Net++	0.954	0.944	0.945
MLT	0.952	0.942	0.942
CNN-Clustering	0.949	0.939	0.938
Chain code-SVM	0.944	0.934	0.935
Inf-Net	0.943	0.932	0.932
R2U-Net	0.939	0.928	0.927
FCN	0.937	0.924	0.923
CPMC	0.931	0.921	0.921

suppresses the noise well. Then, by introducing spatial gravity model and spatial structure characteristics into MRF, a MRF with adaptive spatial information is constructed to overcome the shortcomings of traditional FCM. It can adaptively determine the influence weight of the spatial neighborhood and has good clustering effect for small target areas. It can automatically balance the effectiveness of being insensitive to noise and preserving the edge details of GGO COVID-19 CT images. Finally, by improving the random walk algorithm, it makes full use of the spatial distance relationship between pixel and seed points, and it adds the geodesic distance to classify pixels more accurately. It makes up for the traditional GGO segmentation method based on gray information or Euclidean distance, resulting in the error segmentation of GGO. It ensures the accurate segmentation for different types of GGO lesion areas on CT images. By comparing the segmentation results of the paper method with those of several traditional segmentation algorithms and the SOTA methods based on deep learning, it is proved that the paper method not only improves the segmentation accuracy, but also has good segmentation performance. The paper method can provide doctors with different types of real regions of GGO, with high accuracy of segmentation, which can further improve the accuracy of doctors' diagnosis for COVID-19. The subsequent research of this paper is mainly to optimize the performance of the algorithm. The adaptive parameters of the snowfall model need to be further improved to increase the segmentation integrity of the complex images. The seed points extraction of the random walk needs to be further advanced to improve the quality of the image segmentation.

CRediT authorship contribution statement

Guowei Wang: Writing – original draft, Methodology, Software, Investigation, Validation. **Shuli Guo:** Conceptualization. **Lina Han:** Writing – review & editing. **Zhilei Zhao:** Data curation. **Xiaowei Song:** Visualization.

Declaration of competing interest

The authors declare that they have no known competing financial interests or personal relationships that could have appeared to influence the work reported in this paper.

Data availability

Data will be made available on request.

Acknowledgments

This research has been funded by Beijing Natural Science Foundation, China (L192064, M21018) and Hainan Province Science and Technology Special Fund, China under Grant ZDYF2021GXJS205.

References

[1] Guowei Wang, Shuli Guo, Lina Han, Anil Baris Cekderi, Xiaowei Song, Zhilei Zhao, Asymptomatic COVID-19 CT image denoising method based on wavelet transform combined with improved PSO, Biomed. Signal Process. Control 76 (2022) 103707.
[2] Essam H. Houssein, Marwa M. Emam, Abdelmgeid A. Ali, Improved manta ray foraging optimization for multi-level thresholding using COVID-19 CT images, Neural Comput. Appl. 33 (2021) 16899–16919.
[3] Guowei Wang, Shuli Guo, Lina Han, Anil Baris Cekderi, Two-dimensional reciprocal cross entropy multi-threshold combined with improved firefly algorithm for lung parenchyma segmentation of COVID-19 CT image, Biomed. Signal Process. Control 78 (2022) 103933.
[4] Mohammad Rahimzadeh, Abolfazl Attar, Mohammad Sakhaei, A fully automated deep learning-based network for detecting COVID-19 from a new and large lung CT scan dataset, Biomed Signal Proc,. Control (2020).
[5] SeyyedMohammad JavadiMoghaddam, Hossain Gholamalinejad, A novel deep learning based method for COVID-19 detection from CT image, Biomed. Signal Process. Control 70 (2021) 102987.
[6] Prasad Kalane, Sarika B. Patil, B. Patil, Davinder Pal Sharma, Automatic detection of COVID-19 disease using U-Net architecture based fully convolutional network, Biomed. Signal Process. Control 67 (2021) 102518.
[7] Adel Oulefki, Sos S. Agaian, Thaweesak Trongtirakul, Samir Benbelkacem, Djamel Aouam, Nadia Zenati-Henda, Mohamed-Lamine Abdelli, Virtual Reality visualization for computerized COVID-19 lesion segmentation and interpretation, Biomed. Signal Process. Control 73 (2021) 103371.
[8] Shouvik Chakraborty, Kalyani Mali, A radiological image analysis framework for early screening of the COVID-19 infection: A computer vision-based approach, Appl. Soft Comput. 119 (2022) 108528.
[9] Tapan Behl, Ishnoor Kaur, Lotfi Aleya, Aayush Sehgal, Sukhbir Singh, Neelam Sharma, Saurabh Bhatia, Ahmed Al-Harrasi, Simona Gabriela Bungu, CD147-spike protein interaction in COVID-19: Get the ball rolling with a novel receptor and therapeutic target, Sci. Total Environ. 808 (2021) 152072.
[10] Dong Liu, Sacha Epskamp, Adela-Maria Isvoranu, Cai wang Chen, Wenjun Liu, Xinyi Hong, Network analysis of physical and psychiatric symptoms of hospital discharged patients infected with COVID-19, J. Affect. Disord. 294 (2021) 707–713.
[11] Haseeb Hassan, Zhaoyu Ren, Chengmin Zhou, Muazzam A. Khan, Yi Pan, Jian Zhao, Bingding Huang, Supervised and weakly supervised deep learning models for COVID-19 CT diagnosis: A systematic review, Comput. Methods Programs Biomed. 218 (2022) 106731.
[12] Dong Wei, Yongjun Zhang, Chang Li, Robust line segment matching via reweighted random walks on the homography graph, Pattern Recognit. 111 (2021) 107693.
[13] Hui Wang, Weibin Liu, Weiwei Xing, Video object segmentation via random walks on two-frame graphs comprising superpixels, J. Vis. Commun. Image Represent. 80 (2021) 103293.
[14] Honghui Fan, Hongjin Zhu, Preservation of image edge feature based on snowfall model smoothing filter, EURASIP J. Image Video Process. 2018 (2018) 1–9.
[15] Ju Zhang, Lunduan Yu, Decheng Chen, Weidong Pan, Chaojun Shi, Yan Niu, Xinwei Yao, Xiaobing Xu, Yun Cheng, Dense GAN and multi-layer attention based lesion segmentation method for COVID-19 CT images, Biomed. Signal Process. Control 69 (2021) 102901.
[16] Abolfazl Kouhi, Hadi Seyedarabi, Ali Aghagolzadeh, Robust FCM clustering algorithm with combined spatial constraint and membership matrix local information for brain MRI segmentation, Expert Syst. Appl. 146 (2020) 113159.
[17] Racine A. Basant, Graham A. Ryan, Jared R. Peacock, Antonio G. Camacho, O.O. Blake, Stefan H. Hautmann, Bridget Y. Lynne, Multi-geophysical parameter classification of the Montserrat geothermal system, Geothermics 90 (2021) 102006.
[18] Pranaba K. Mishro, Sanjay Agrawal, Rutuparna Panda, Ajith Abraham, A novel type-2 fuzzy C-means clustering for brain MR image segmentation, IEEE Trans. Cybern. 51 (2021) 3901–3912.
[19] Lei Hua, Yi Gu, Xiaoqing Gu, Jing Xue, Tongguang Ni, A novel brain MRI image segmentation method using an improved multi-view fuzzy c-means clustering algorithm, Front. Neurosci. 15 (2021).
[20] Simon Tongbram, Benjamin A. Shimray, Loitongbam Surajkumar Singh, Nameirakpam Dhanachandra, A novel image segmentation approach using fcm and whale optimization algorithm, J. Ambient Intell. Humaniz. Comput. (2021) 1–15.
[21] Yu Wang, Yuanjun Wang, Anisotropic diffusion filtering method with weighted directional structure tensor, Biomed. Signal Process. Control. 53 (2019).
[22] Erik Valdemar Cuevas Jiménez, Héctor M. Becerra, Alberto Luque, Anisotropic diffusion filtering through multi-objective optimization, Math. Comput. Simulation 181 (2021) 410–429.
[23] Hongjin Ma, Yufeng Nie, Mixed noise removal algorithm combining adaptive directional weighted mean filter and improved adaptive anisotropic diffusion model, Math. Probl. Eng. (2018).
[24] S. Prabha, C.M. Sujatha, Proposal of index to estimate breast similarities in thermograms using fuzzy C means and anisotropic diffusion filter based fuzzy C means clustering, Infrared Phys. Technol. (2018).
[25] Yi Zhang, Mingming Jin, Gang Huang, Medical image fusion based on improved multi-scale morphology gradient-weighted local energy and visual saliency map, Biomed. Signal Process. Control. 74 (2022) 103535.
[26] Shouvik Chakraborty, Kalyani Mali, A morphology-based radiological image segmentation approach for efficient screening of COVID-19, Biomed. Signal Process. Control 69 (2021) 102800.
[27] Arunita Das, Amrita Namtirtha, Animesh Dutta, Fuzzy clustering of acute lymphoblastic leukemia images assisted by Eagle strategy and morphological reconstruction, Knowl.-Based Syst. 239 (2022) 108008.
[28] Cong Xu, Jingru Sun, Chunhua Wang, An image encryption algorithm based on random walk and hyperchaotic systems, Int. J. Bifurc. Chaos 30 (2020) 2050060:1–2050060:16.
[29] Ahmed M. Anter, Diego Oliva, Anuradha D. Thakare, Zhiguo Zhang, AFCM-lsma: New intelligent model based on Lévy slime mould algorithm and adaptive fuzzy C-means for identification of COVID-19 infection from chest X-ray images, Adv. Eng. Inf. 49 (2021) 101317.
[30] S. Triambak, D.P. Mahapatra, A random walk Monte Carlo simulation study of COVID-19-like infection spread, Physica A 574 (2021) 126014.
[31] Tobias Fechter, Sonja Adebahr, Dimos Baltas, Ismail ben Ayed, Christian Desrosiers, José Dolz, Esophagus segmentation in CT via 3D fully convolutional neural network and random walk, Med. Phys. 44 (2017) 6341–6352.
[32] Nilanjan Dey, Venkatesan Rajinikanth, Simon James Fong, Mark S. Kaiser, Mufti Mahmud, Social group optimization–assisted kapur's entropy and morphological segmentation for automated detection of COVID-19 infection from computed tomography images, Cogn. Comput. 12 (2020) 1011–1023.
[33] Ye Yuan, Yen-Wei Chen, Chunhua Dong, Hai Yu, Zhiliang Zhu, Hybrid method combining superpixel, random walk and active contour model for fast and accurate liver segmentation, Comput. Med. Imaging Graph. : Off. J. Comput. Med. Imaging Soc. 70 (2018) 119–134.
[34] Cheng-Fan Li, Yi-Duo Xu, Xue-Hai Ding, Junping Zhao, Rui-Qi Du, Li-Zhong Wu, Wenxiang Sun, MultiR-Net: A novel joint learning network for COVID-19 segmentation and classification, Comput. Biol. Med. 144 (2022) 105340.
[35] Abhishek Dixit, Ashish Mani, Rohit Bansal, CoV2-detect-net: Design of COVID-19 prediction model based on hybrid DE-PSO with SVM using chest X-ray images, Inform. Sci. 571 (2021) 676–692.
[36] R. Karthik, R. Menaka, M. Hariharan, Daehan Won, Contour-enhanced attention CNN for CT-based COVID-19 segmentation, Pattern Recognit. 125 (2022) 108538.
[37] Shairaz Baksh, Natalia V Volodko, Merle Soucie, Sheena Brandon Geier, Anthony Diep, Kallie Rozak, Tak Yin Chan, Jelili Olaide Mustapha, Raymond Lai, Mathew P. Estey, Bob Verity, Mao-Cheng Lee, Extractionless nucleic acid detection: a high capacity solution to COVID-19 testing, Diagn. Microbiol. Infect. Dis. 101 (2021) 115458.
[38] Amir Hossein Barshooi, Abdollah Amirkhani, A novel data augmentation based on Gabor filter and convolutional deep learning for improving the classification of COVID-19 chest X-Ray images, Biomed. Signal Process. Control 72 (2021) 103326.
[39] Mingde Zhao, Yang Wei, Yu Lu, Kelvin Kian Loong Wong, A novel U-Net approach to segment the cardiac chamber in magnetic resonance images with ghost artifacts, Comput. Methods Programs Biomed. 196 (2020) 105623.
[40] Junjie Hu, Ying Song, Lei Zhang, Sen Bai, Zhang Yi, Multi-scale attention U-net for segmenting clinical target volume in graves' ophthalmopathy, Neurocomputing 427 (2021) 74–83.
[41] Hemalatha Munusamy, J. Karthikeyan, G. Shriram, S. Thanga Revathi, S. Aravindkumar, FractalCovNet architecture for COVID-19 chest X-ray image classification and CT-scan image segmentation, Biocybern. Biomed. Eng. 41 (2021) 1025–1038.
[42] Hongyuan Zhu, Fanman Meng, Jianfei Cai, Shijian Lu, Beyond pixels: A comprehensive survey from bottom-up to semantic image segmentation and cosegmentation, J. Vis. Commun. Image Represent. 34 (2016) 12–27.